

## Synthesis under hydrothermal conditions and structural transformations of nanocrystals in the $\text{LaPO}_4\text{--YPO}_4\text{--(H}_2\text{O)}$ system

Maria O. Enikeeva<sup>1,2,a</sup>, Olga V. Proskurina<sup>1,2,b</sup>, Evgeny Yu. Gerasimov<sup>3,c</sup>,  
Vladimir N. Nevedomskiy<sup>1,d</sup>, Victor V. Gusarov<sup>1,e</sup>

<sup>1</sup>Ioffe Institute, 194021 St. Petersburg, Russia

<sup>2</sup>St. Petersburg State Institute of Technology, 190013 St. Petersburg, Russia

<sup>3</sup>Federal Research Center, Boreskov Institute of Catalysis SB RAS, Novosibirsk 630090, Russia

<sup>a</sup>odin2tri45678@gmail.com, <sup>b</sup>proskurinaov@mail.ru, <sup>c</sup>gerasimov@catalysis.ru,

<sup>d</sup>nevedom@mail.ioffe.ru, <sup>e</sup>gusarov@mail.ioffe.ru

Corresponding author: M. O. Enikeeva, [odin2tri45678@gmail.com](mailto:odin2tri45678@gmail.com)

**ABSTRACT** Structural transformations of nanocrystals in the  $\text{LaPO}_4\text{--YPO}_4\text{--(H}_2\text{O)}$  oxide system were investigated under hydrothermal conditions at 230°C, depending on isothermal holding times (2 hours, 7 days and 28 days). It was shown that before hydrothermal processing, phases crystallize in the system with rhabdophane structures  $\text{La}_{1-x}\text{Y}_x\text{PO}_4 \cdot n\text{H}_2\text{O}$  ( $0 \leq x \leq 0.80$ ) and xenotime  $\text{YPO}_4$ . It has been determined that increasing the duration of isothermal treatment under hydrothermal conditions leads to the transformation of the rhabdophane phase into phases with monazite and equilibrium xenotime structures, with an intermediate crystallization of the metastable monazite phase. It is noted that only after 28 days of hydrothermal treatment at 230°C, the system approaches the equilibrium composition of the phases with monazite structures  $\text{La}_{0.97}\text{Y}_{0.03}\text{PO}_4$  (with crystal sizes of 18–50 nm) and xenotime  $\text{YPO}_4$  (with crystal sizes of 45–90 nm). In a single-phase sample with a monazite structure  $\text{La}_{0.75}\text{Y}_{0.25}\text{PO}_4$ , the average crystal size remains unchanged at around 20 nm after 2 hours, 7 days and 28 days of hydrothermal treatment at 230°C.

**KEYWORDS** nanocrystals, monazite, xenotime, rhabdophane, structural transformations, yttrium phosphate, lanthanum phosphate.

**ACKNOWLEDGEMENTS** Powder XRD measurements, Rietveld refinement of crystal structures and EDX analysis have been carried out with using the equipment and software of the Engineering Department of the St. Petersburg State University of Technology (Technical University). TEM investigations carried out with using the equipment of the Joint Research Center 'Materials science and characterization in advanced technology' (Ioffe Institute, St. Petersburg) and HRTEM study was carried out using the facilities of the "National center of investigation of catalysts" at Boreskov Institute of Catalysis. The present work of M.O.E., O.V.P. and V.V.G. was supported by the Russian Science Foundation (project no. 21-13-00260).

**FOR CITATION** Enikeeva M.O., Proskurina O.V., Gerasimov E.Yu., Nevedomskiy V.N., Gusarov V.V. Synthesis under hydrothermal conditions and structural transformations of nanocrystals in the  $\text{LaPO}_4\text{--YPO}_4\text{--(H}_2\text{O)}$  system. *Nanosystems: Phys. Chem. Math.*, 2023, **14** (6), 660–671.

### 1. Introduction

Materials based on nanocrystalline rare-earth phosphates are of significant interest due to their wide range of applications in optics [1–4], catalysis [2, 5, 6], medicine [7–9], fabrication of gas sensors [10] and other fields [11–13]. Special attention is given to the binary- and multi-component systems based on rare-earth orthophosphates, as they are used as luminescent materials [14, 15] and matrices for immobilizing toxic and radioactive waste [16–18].

Depending on the synthesis conditions, rare-earth phosphates can be obtained in the form of phases with a monazite structure ( $\text{LREPO}_4$ ,  $\text{LRE}=\text{La}\rightarrow\text{Gd}$ , space group (SG):  $P2_1/n$ ) [19–21], xenotime structure ( $\text{HREPO}_4$ ,  $\text{HRE}=\text{Tb}\rightarrow\text{Lu}$ , Y, Sc; SG:  $I4_1/amd$ ) [19, 21], rhabdophane structure ( $\text{REPO}_4 \cdot n\text{H}_2\text{O}$ ,  $\text{RE}=\text{La}\rightarrow\text{Gd}$ , Y,  $n=0\text{--}1$ ; SG:  $C2$  or  $P6_222$ ) [22, 23] and churchite or weinschenkite structure ( $\text{HREPO}_4 \cdot 2\text{H}_2\text{O}$ ,  $\text{HRE}=\text{Tb}\rightarrow\text{Lu}$ , Y; SG:  $C2/c$ ) [24–26]. Hydrated phases with rhabdophane and churchite structures are often considered as precursors for the formation of anhydrous phases with monazite and xenotime structures. It was found that the loss of structurally bound water with increasing temperature leads to the transition of the rhabdophane structure to monazite and the churchite structure to xenotime for individual compounds of the  $\text{REPO}_4 \cdot n\text{H}_2\text{O}$  type [27, 28]. An exception is yttrium orthophosphate, which crystallizes under certain conditions into a phase with a rhabdophane structure that can transform into a phase with a xenotime structure [29]. However, it is also possible to form anhydrous phases with monazite and xenotime structures without the use of high temperatures [30, 31].

For the synthesis of nanocrystalline materials based on rare-earth orthophosphates, soft chemistry methods are commonly used, such as precipitation [28, 32–34], sol-gel [3, 35–38], hydrothermal and hydrothermal-microwave synthesis [1, 4, 38–41]. At times, precipitates obtained by soft chemistry methods are annealed at temperatures  $\geq 500^\circ\text{C}$  to obtain samples with monazite and xenotime structures [18, 20, 43].

Studies of structural transformations in the  $\text{LaPO}_4\text{--YPO}_4\text{--}(\text{H}_2\text{O})$  system were investigated in works [34, 36, 44–49]. During heat treatment at temperatures of  $1000\text{--}1600^\circ\text{C}$ , phases with monazite and xenotime structures are formed in the system. There is a wide homogeneity range of solid-solution with a monazite structure (up to 42 mol. %  $\text{YPO}_4$  at  $T = 1600^\circ\text{C}$ ), while the solubility of  $\text{LaPO}_4$  in the xenotime phase is extremely low (less than a few percent at  $T = 1600^\circ\text{C}$ ). Phases with rhabdophane, monazite and xenotime structures were obtained in the  $\text{LaPO}_4\text{--YPO}_4\text{--H}_2\text{O}$  system using soft chemistry synthesis methods. However, research in the low-temperature range remains poorly systematic and has little focus on phase transformations in the system with varying synthesis durations. This information can be valuable for improving the understanding of phase stability in the  $\text{LaPO}_4\text{--YPO}_4\text{--H}_2\text{O}$  system and predicting the behavior of functional materials based on it.

Taking into account the above considerations, this study aims to investigate the structural transformations of nanocrystals in the oxide system  $\text{LaPO}_4\text{--YPO}_4\text{--}(\text{H}_2\text{O})$  under hydrothermal conditions, focusing on the influence of the duration of isothermal holding times.

## 2. Experimental

The following chemical reagents were used for the synthesis of nanopowders with the composition  $\text{La}_{1-x}\text{Y}_x\text{PO}_4 \cdot n\text{H}_2\text{O}$  ( $x = 0\text{--}1$ ): lanthanum (III) nitrate hexahydrate  $\text{La}(\text{NO}_3)_3 \cdot 6\text{H}_2\text{O}$  (puriss.), yttrium (III) nitrate hexahydrate  $\text{Y}(\text{NO}_3)_3 \cdot 6\text{H}_2\text{O}$  (puriss.) and ammonium dihydrogen phosphate  $\text{NH}_4\text{H}_2\text{PO}_4$  (puriss.).

The precipitation was carried out from solutions of the reagents in distilled water by adding the  $\text{NH}_4\text{H}_2\text{PO}_4$  solution to the rare-earth nitrate solution with continuous stirring at  $T = 25 \pm 5^\circ\text{C}$ . The resulting white suspension with  $\text{pH}=1$  was constantly stirred for 15 minutes.

For hydrothermal synthesis, the suspension obtained by precipitation was transferred into a Teflon-lined autoclave (filling factor 0.7) and hydrothermally treated at  $T = 230^\circ\text{C}$  and  $P \sim 10$  MPa with isothermal holding times: 2 hours, 7 days and 28 days.

Samples obtained by both precipitation and hydrothermal treatment were washed with distilled water until reaching a  $\text{pH}$  of 7, centrifuged (at 10,000 rpm), dried at  $T = 75^\circ\text{C}$  for 24 hours and subsequently ground using an agate mortar.

The elemental composition of the samples was determined using energy-dispersive X-ray spectroscopy (EDS) with a Tescan Vega 3 SBH scanning electron microscope (Tescan, Czech Republic) equipped with an Oxford Instruments INCA x-act microanalysis system (UK). The measurements were conducted in the energy range up to 20 keV in five different areas and the obtained values were averaged.

X-ray diffraction (XRD) analysis of the samples was performed based on the powder diffraction patterns obtained using a Rigaku SmartLab 3 X-ray diffractometer ( $\text{Cu } K\alpha$ -radiation) in the angular range of  $2\theta = 10\text{--}90^\circ$  with a step size of  $0.01^\circ$  and scan speeds of  $0.2^\circ/\text{min}$  and  $0.8^\circ/\text{min}$ . Phase analysis of the samples was carried out using the ICSD PDF-2 and CSD databases. Quantitative phase analysis was performed using the *SmartLab Studio SmartLab Studio II* v4.4.241.0 (Rigaku Corporation, Japan). The average crystallite sizes were determined using non-overlapping reflections for each phase: the 200 reflection for the monazite structure phase, the 101 reflection for the xenotime structure phase and the  $11\bar{1}$  reflection for the rhabdophane structure phase. The average crystallite size of xenotime phase in the samples obtained by precipitation was determined using the Scherrer formula [50] based on 101 and 200 reflections. The composition of the variable composition phase with a monazite structure was determined using Retgers law [51] and literature data [20, 46].

The investigation of the crystal structure and microstructure of the samples was carried out using high-resolution transmission electron microscopy (HRTEM) on an electron microscope ThemisZ (Thermo Fisher Scientific, USA), which provided a maximum lattice resolution of 0.07 nm and on an electron microscope JEM- 2100F (JEOL Ltd., Akishima, Tokyo, Japan) with an accelerating voltage of 200 kV. During the operation of the ThemisZ microscope, images were recorded using a Ceta 16 CCD sensor (Thermo Fisher Scientific, USA). The microscope ThemisZ was also equipped with an EDX Super-X spectrometer (Thermo Fisher Scientific, Bleiswijk, The Netherlands) with a semiconductor Si detector providing an energy resolution of 128 eV.

To construct particle size distribution histograms, particle images were analyzed by the *ImageJ* software. There were at least 40 particles in the samples. The distribution histogram was processed using the lognormal distribution law.

## 3. Results and discussions

According to the elemental analysis data, the molar ratio of RE:P is close to 1:1 in all samples, which corresponds to the stoichiometry of rare-earth phosphate. For the designation of the samples, an experimentally determined molar ratio of yttrium and lanthanum is used, expressed as  $\text{Y}n\%$ , where  $n\% = n(\text{Y}) / (n(\text{Y}) + n(\text{La})) \cdot 100\%$ .  $\text{Y}n\%$  - represents the molar percentage of yttrium relative to the sum of rare-earth elements,  $n(\text{Y})$  is the molar fraction of yttrium in the sample and  $n(\text{La})$  is the molar fraction of lanthanum in the sample.

Figure 1 shows the X-ray diffraction patterns of the samples obtained by precipitation. Nanocrystalline samples with compositions of 0%–Y73% exhibit a rhabdophane structure. In the Y81% sample, reflections of the rhabdophane structure are present, as well as broadened reflections corresponding to the xenotime structure, which are also observed in the Y93%–Y100% samples.

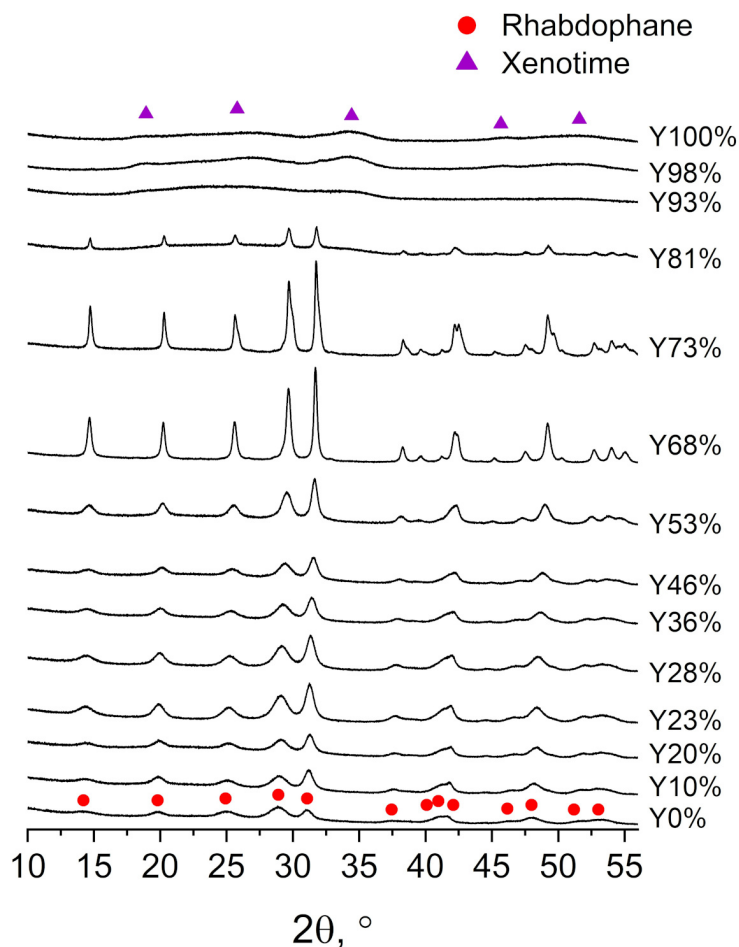


FIG. 1. The X-ray diffraction patterns of the samples obtained by precipitation

Figure 2(a) present the dependency of the unit cell volume per formula unit on the composition of the system for the rhabdophane and xenotime structure phases in the samples obtained by precipitation method. In the system, a solid solution with a rhabdophane structure  $\text{La}_{1-x}\text{Y}_x\text{PO}_4 \cdot n\text{H}_2\text{O}$  ( $x < 0.81$ ) is formed. In the Y81% sample, the obtained values of the  $V/z$  parameter for the rhabdophane structure have larger values compared to those for the Y73% sample, which is due to the crystallization of the  $\text{YPO}_4$  xenotime-structured phase in this sample as well. The presence of an amorphous phase containing lanthanum cannot be excluded in the Y93%–Y98% samples.

The dependence of the weighted average crystallite size with rhabdophane structure on the  $\text{YPO}_4$  content in the system is shown in Fig. 2(b). For  $\text{La}_{1-x}\text{Y}_x\text{PO}_4 \cdot n\text{H}_2\text{O}$  ( $x < 0.5$ ), the formation of nanocrystals with an average size of 5–10 nm. Further increase in the molar fraction of yttrium orthophosphate in the system leads to an increase in the sizes of rhabdophane-structured crystals several times. In the Y81% sample, the value  $D = 45 \pm 30$  nm. The average size of xenotime-structured phase crystals in Y93%–Y100% samples, determined by the Scherrer formula, does not exceed 5 nm.

Figure 3(a,c,e) present microphotographs of Y23%, Y73% and Y100% nanoparticles obtained by precipitation method. Microphotographs for the  $\text{LaPO}_4$  sample obtained by precipitation method are presented in the work [32]. Based on the analysis of the images, histograms of particle size distribution according to their cross-sectional area (thickness) were constructed, as shown in the Appendix (Supporting Materials Fig. S1(a,b,c)). The Y23% nanoparticles with rhabdophane structure have a rod-like shape (Fig. 2(a)) with a narrow distribution of particle thicknesses (Fig. S1(a)). The thickness of the nanorods varies in the range of 5–10 nm.

In the Y73% sample (Fig. 3(c)), the particles have an prolate form with a significantly lower aspect ratio of geometric parameters compared to the  $\text{LaPO}_4$  sample [32]. The particle size distribution for the Y73% sample with rhabdophane structure, shown in Fig. S1(b), is considerably wider than that of the Y23% sample. The particle thickness varies in the

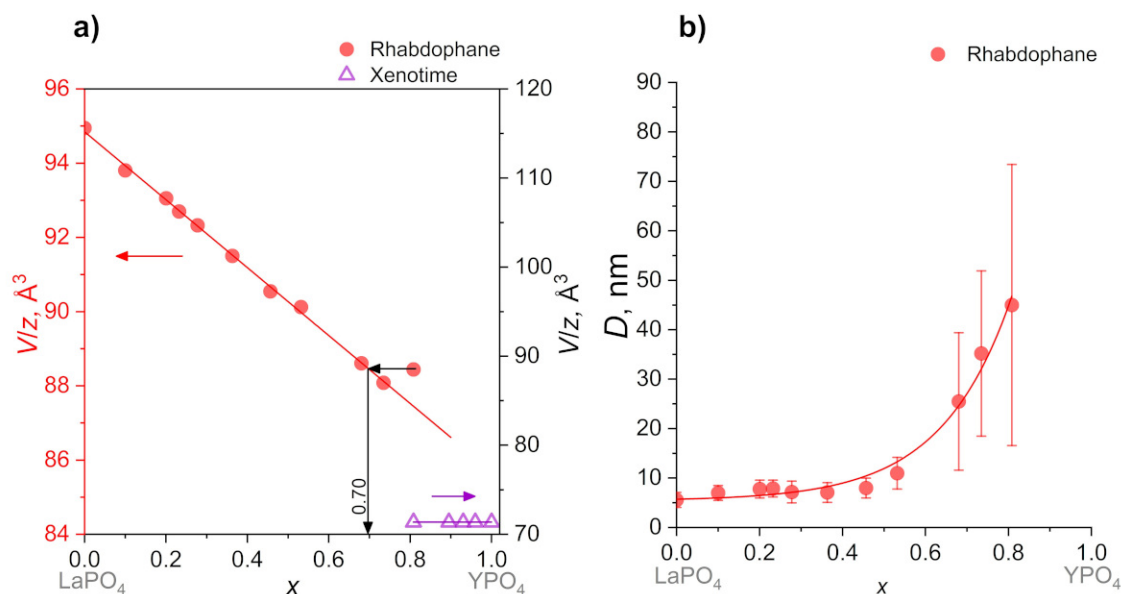


FIG. 2. a) The dependence of unit cell per formula unit of structure on the yttrium content; b) The mean volume weighted crystallite size ( $D$ ) of the rhabdophane-structured nanocrystals  $\text{La}_{1-x}\text{Y}_x\text{PO}_4 \cdot n\text{H}_2\text{O}$  ( $x \leq 0.81$ ), obtained by precipitation method, on the composition of the system

range of 10 to 50 nm. The average crystal sizes for the Y23% and Y73% samples (Fig. 2(b)) with rhabdophane structure correlate quite well with the average particle thicknesses (Fig. S1(a,b)) of these samples. This was also shown in the work [45] for samples with the composition  $\text{LaPO}_4:\text{YPO}_4=1:3$ .

In the Y100% sample (Fig. 3(e)), there are nanocrystals with interplanar distances  $d \approx 3.45 \text{ \AA}$  and  $d \approx 2.56 \text{ \AA}$  corresponding to the (200) and (112) planes of the xenotime structure. The cross-sectional size of the nanoparticles in the sample does not exceed 10 nm (distribution shown in Fig. S1(c)) and correlates with the crystal size of the xenotime-structured phase, as determined by the Scherrer formula ( $\sim 5 \text{ nm}$ ).

The microdiffraction patterns of the Y23%, Y73% and Y100% samples are shown in Fig. 3(b,d,f). In the Y23% and Y73% samples, only rhabdophane structure reflections are observed, while in the Y100% sample, only xenotime-structured phase reflections are presented.

Figure 4(a) shows a microphotograph of particles from the Y73% sample with rhabdophane structure, synthesized by precipitation method. The results of elemental mapping are shown in Fig. 4(b). Despite the Y73% sample with rhabdophane structure being single-phase, the distribution of elements  $\text{La}(L_{\alpha}\text{-series})$  and  $\text{Y}(K_{\alpha}\text{-series})$  in each particle is not homogeneous. Energy-dispersive analysis of an individual particle showed that the Y:La ratio at the edges of the particle is close to 4:1, while in the central part of the particle, it is approximately 3:2. The total amount of yttrium in all particles corresponds to the composition determined by energy-dispersive X-ray analysis using SEM, i.e., close to 73 mol.%  $\text{YPO}_4$ . Apparently, the compositional inhomogeneity of the particles in the Y73% sample can be attributed to the difference in the solubility product of lanthanum and yttrium phosphates in an acidic media. This leads to the formation of nanocrystals with a rhabdophane structure containing a relatively higher amount of La than indicated by the stoichiometry of the precipitated phase. As a result, the mother liquid becomes depleted in  $\text{La}^{3+}$  ions and an yttrium-enriched rhabdophane phase crystallizes on the periphery of the particles. Fig. S2 shows the image of an individual particle from the Y73% sample with complete elemental mapping, where the presence of lanthanum can also be observed predominantly in the central part of the particle.

In the  $\text{LaPO}_4\text{-YPO}_4\text{-(H}_2\text{O)}$  system, after hydrothermal treatment (HT) at  $230^\circ\text{C}$  with different isothermal holding times (2 hours, 7 days and 28 days), phases with monazite, rhabdophane and xenotime structures crystallize. The diffraction patterns of the samples are presented in the Supporting Materials in Fig. S3, S4 and S5.

The phase quantities and the dependence of the unit cell per formula unit of structure on the yttrium content after hydrothermal treatment are shown in Fig. 5(a-f). HT of samples for 2 hours (Fig. 5(a,b)) leads to the formation of a solid solution with a monazite structure  $\text{La}_{1-x}\text{Y}_x\text{PO}_4$  ( $x \leq 0.38$ ), the formation of a solid solution with a rhabdophane structure and the formation of a phase with a xenotime structure. The single-phase solid solution with a monazite structure has a composition of  $0 < x \leq 0.25$ . Partial phase transformation the rhabdophane structure to the monazite structure occurs in the samples  $0.25 < x < 0.70$ , which is consistent with the data on the  $\text{LaPO}_4:\text{YPO}_4=1:1$  sample obtained under hydrothermal-microwave conditions [49]. In samples Y71%–Y80%, one phase with the rhabdophane structure is formed, similar to before HT (Fig. 2(a)). For samples with a composition of  $0.85 \leq x \leq 0.92$  after 2 hours of HT, the initial precipitate, which contains not only amorphous phase but also nanocrystalline xenotime, transforms into phases with

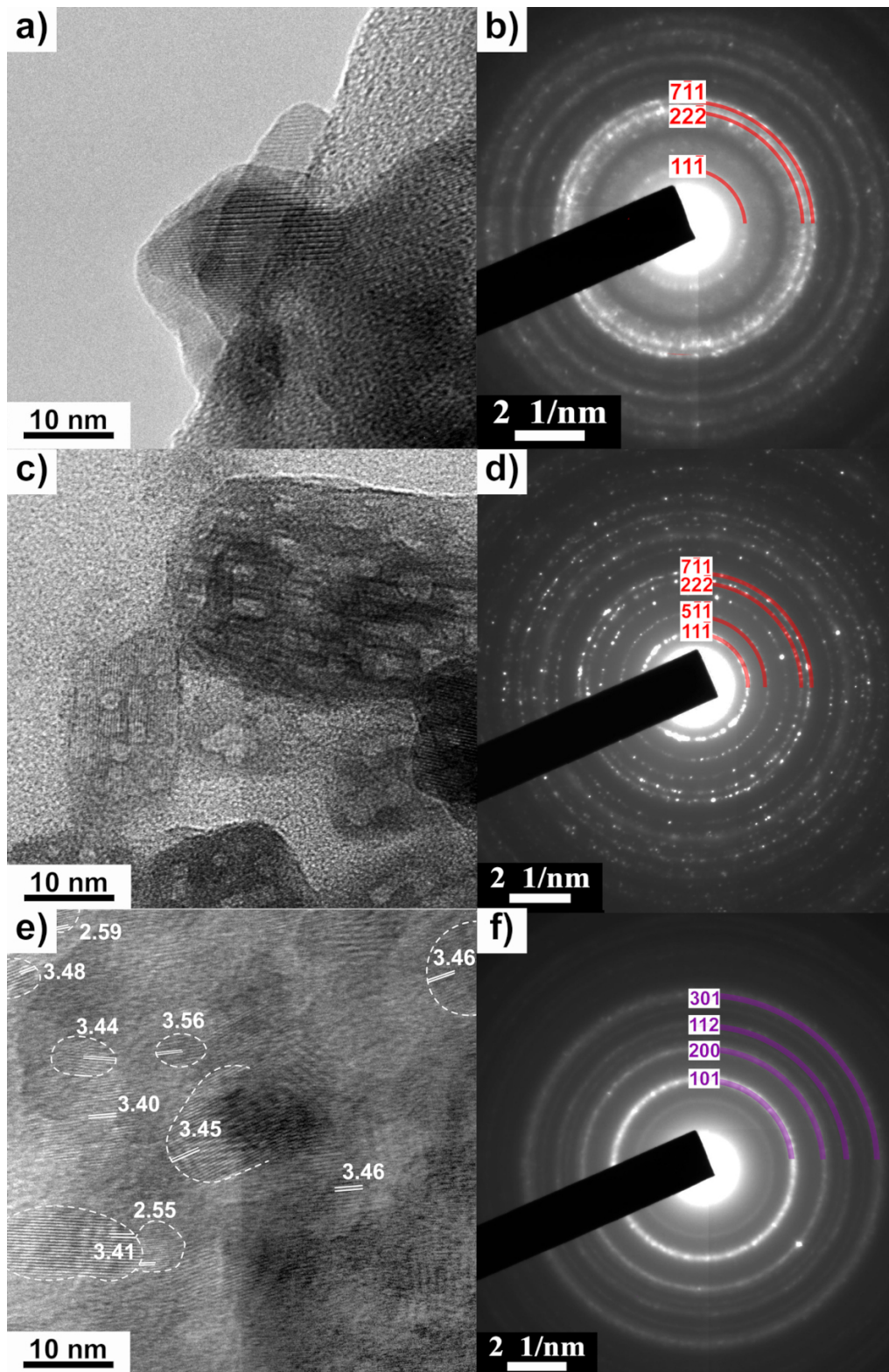


FIG. 3. TEM images and microdiffraction patterns samples synthesized by precipitation method: a,b) Y23%; c,d) Y73% and e,f) Y100% (YPO<sub>4</sub>)

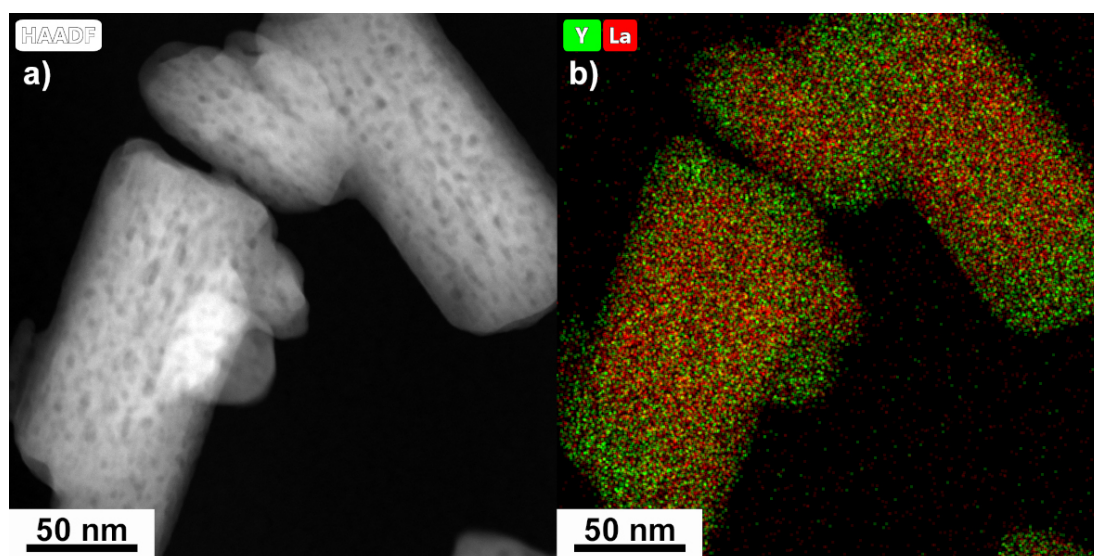


FIG. 4. a) TEM image and b) element mapping particles from the Y73% sample, synthesized by precipitation method

structures of monazite, rhabdophane and xenotime. The monazite phase is depleted in  $\text{YPO}_4$  component compared to the nominal composition of the samples and has the composition  $\text{La}_{1-x}\text{Y}_x\text{PO}_4$  ( $x \leq 0.28$ ). The fraction of monazite phase in samples containing  $0.85 \leq x \leq 0.92$  is approximately 10%. The composition of the xenotime phase can be considered close to  $\text{YPO}_4$  within the experimental error. The composition of the rhabdophane phase  $\text{La}_{1-x}\text{Y}_x\text{PO}_4 \cdot n\text{H}_2\text{O}$  is difficult to determine accurately due to the narrow concentration range of a single-phase region after hydrothermal treatment. The fraction of xenotime phase in samples with a composition of  $0.85 \leq x \leq 0.92$  increases along with the fraction of yttrium phosphate in the system. In samples Y97% and Y100%, only the xenotime phase is observed in the diffraction patterns.

Figure 5(c,d) shows the phase ratios and changes in the unit-cell volume normalized to the number of formula units for the monazite and xenotime phases in samples after 7 days of HT. The samples have completely transformed from the rhabdophane structure to phases with monazite and xenotime structures. For samples with a composition of  $x \leq 0.25$ , the formation of the solid solution with a monazite structure is observed, similar to that after 2 hours of HT. Samples Y53%, Y74% and Y84% contain two phases with different compositions but with a monazite structure, as well as a phase with a xenotime structure. The diffraction patterns of the samples, presented in Fig. S4, show reflections of two monazite phases with the different dissolved yttrium, as well as reflections of the xenotime structure. For the Y53% sample, the profiles of the reflections of the two monazite phases heavily overlap, indicating their similar composition and a relatively large error in determining the parameters of the unit cell. In the Y74% and Y84% samples, the fraction of the monazite phase enriched in yttrium, with a composition of  $0.28 \leq x \leq 0.37$ , does not exceed 30% and decreases with an increase in the amount of yttrium in the system. The fraction of the second monazite phase, with a composition of  $0.09 \leq x \leq 0.12$ , does not exceed 8%.

The phase ratios and changes in the volume of the unit cell, normalized to one formula unit, for the monazite and xenotime phases in samples after 28 days of HT, are shown in Fig. 5(e,f). Samples Y54%, Y74% and Y84% contain a xenotime phase and a single phase with a variable composition monazite structure. The phase ratio in the entire two-phase region has a linear character, indicating a nearly equilibrium phase ratio in the  $\text{LaPO}_4\text{--YPO}_4\text{--}(\text{H}_2\text{O})$  system. It is worth noting that the composition of the monazite phase  $\text{La}_{1-x}\text{Y}_x\text{PO}_4$  ( $x \approx 0.03$ ) in the Y84% sample can be considered as the closest to the equilibrium at  $T = 230^\circ\text{C}$ ,  $P \sim 10$  MPa (hydrothermal conditions). At compositions closer to this ratio of  $\text{LaPO}_4\text{:YPO}_4$ , phase transformations occur more slowly and in samples after 28 days HT, solid solutions with a monazite structure  $\text{La}_{1-x}\text{Y}_x\text{PO}_4$  exist with a composition of  $0.07 \leq x \leq 0.17$ .

The dependencies of the mean volume weighted crystallite size of phases in the samples after 2 hours of HT are shown in Fig. 6(a), after 7 days in Fig. 6(b) and after 28 days in Fig. 6(c). After 2 hours of HT, the crystallites with a monazite structure do not exceed 20 nm in samples with compositions of  $x \leq 0.60$ . The crystallites of the rhabdophane phase, which coexist with the monazite phase, have similar values of the mean crystallite size (around 20 nm). In the single-phase region under these HT conditions, the rhabdophane crystallites reach 80 nm. It should be noted that the dependence of the mean volume weighted crystallite size of the rhabdophane phase after HT-treated similar to samples, obtained by precipitation method and, tends to increase with an increase in the molar fraction of  $\text{YPO}_4$  in the system. The crystallites with a monazite structure in samples Y86%–Y92% exhibit significant variation in size, ranging from 20 to 100 nm. The xenotime phase crystallites have the mean volume weighted size of  $D \approx 60$  nm with a fairly wide range of values.

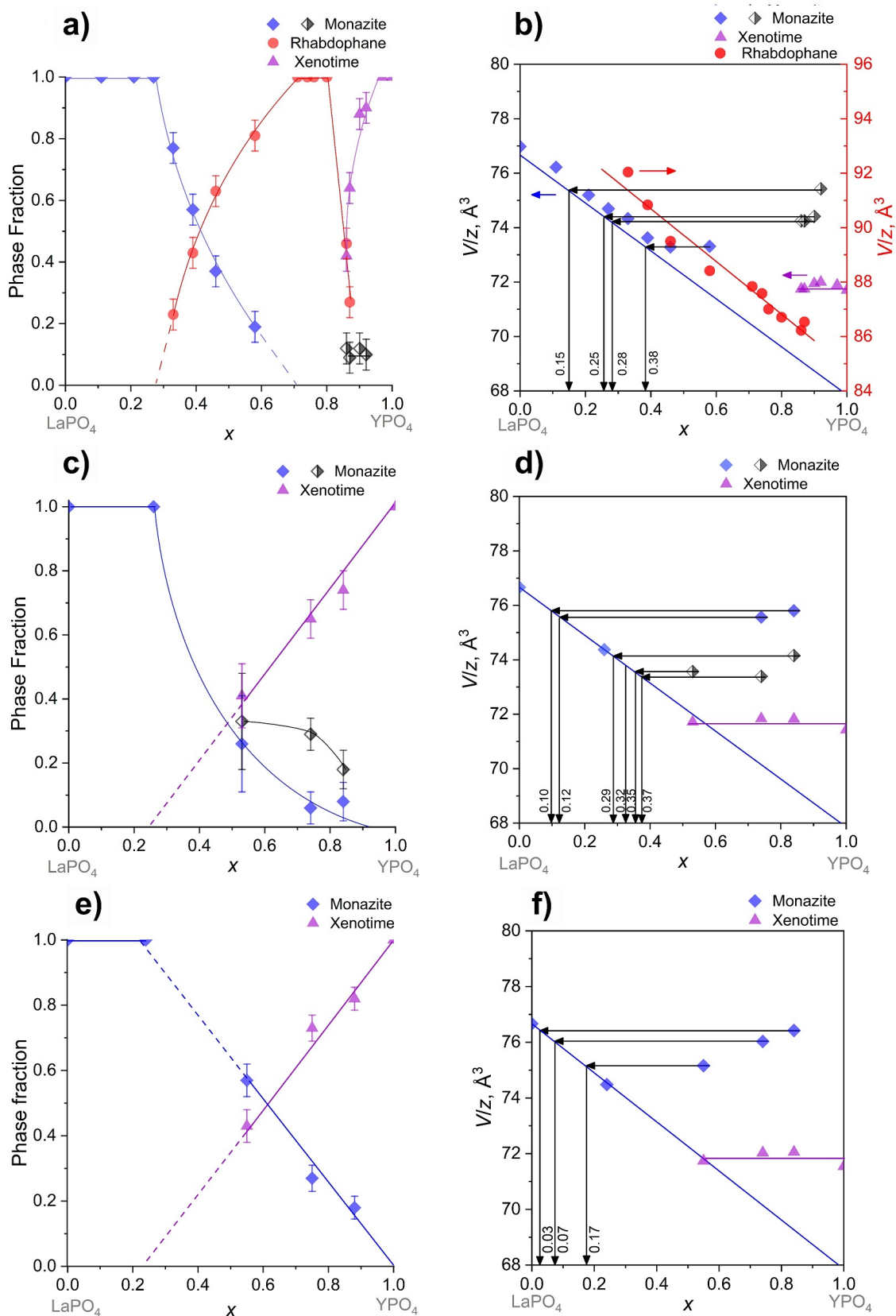


FIG. 5. Phase ratio and change in the unit-cell volume normalized to the number of formula units for rhabdophane, monazite and xenotime structures on the yttrium content of samples after HT: a,b) 2 hours; c,d) 7 days; e,f) 28 days

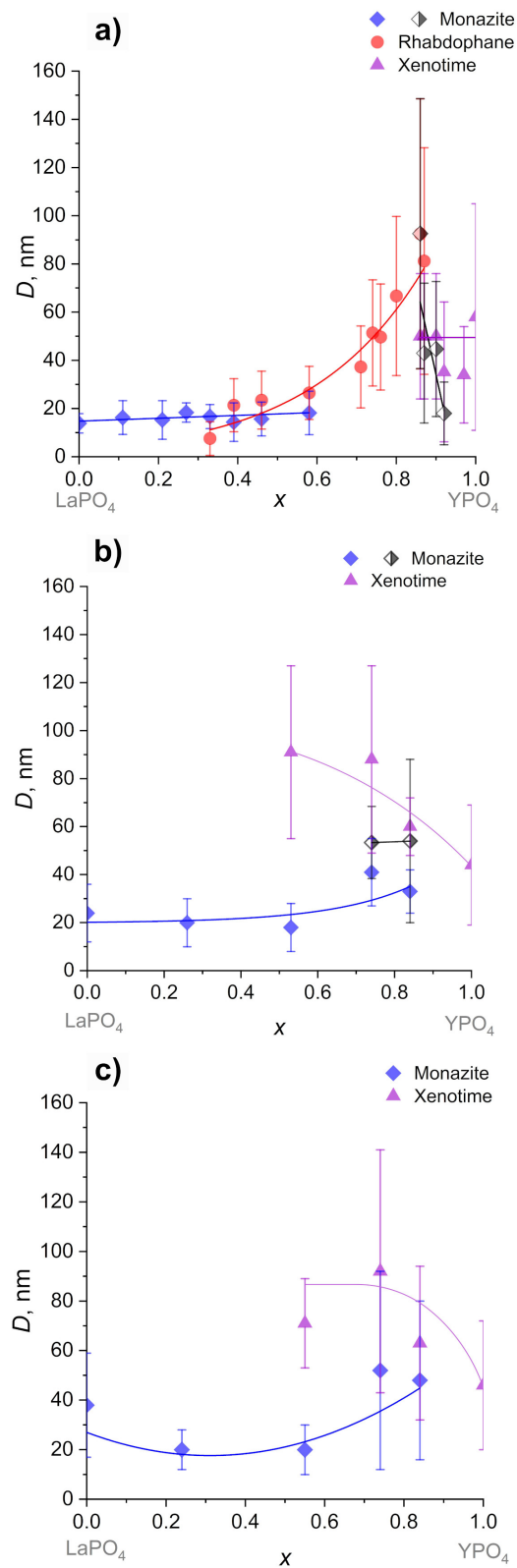


FIG. 6. The dependence of the mean volume weighted crystallite size on the composition of the system of samples after HT: a,b) 2 hours; c,d) 7 days; e,f) 28 days

After 7 days of HT, the mean volume weighted crystallite size of the monazite phase in samples with  $x \leq 0.50$  was found to be  $20 \pm 10$  nm (Fig. 6(b)). In samples with a  $\text{LaPO}_4:\text{YPO}_4$  ratio close to 1:1, there is a tendency for the weighted average crystallite size of the xenotime phase to increase to  $90 \pm 35$  nm compared to the Y100% sample ( $D = 45 \pm 25$  nm). The weighted average crystallite sizes of the monazite phase in the Y74% and Y84% samples are quite close, averaging  $50 \pm 20$  nm. The determination of the average crystallite size of the monazite phase in the Y53% sample has a larger error due to the overlap of two reflections from monazite phases with different compositions. It is worth noting that the crystallite sizes may be smaller than 20 nm for both compositions of the monazite phase.

After 28 days under hydrothermal conditions, the mean volume weighted crystallite size of the monazite phase in the Y0% sample twofold increase compared to that after 2 hours of HT, reaching  $38 \pm 21$  nm. The average crystallite sizes of the xenotime structure in samples with a  $\text{LaPO}_4:\text{YPO}_4$  ratio of approximately 1:1 tend to increase, similar to the samples after 7 days of HT. The decrease value of the mean volume weighted crystallite sizes of the xenotime structure in the Y54% sample is likely caused by the transformation of the metastable phase with a monazite structure into phases with xenotime and monazite structures. As a result of the transformation process, new nanocrystals with a smaller size and a xenotime structure are formed, which affects the size distribution characteristics. The weighted average crystallite sizes of the monazite and xenotime structures in the Y74% and Y84% samples have a larger range of values compared to samples of the same composition after 7 days of HT. This fact is likely also caused by the transformation of the metastable phase with a monazite structure into more stable phases - a monazite phase with a different composition and a xenotime phase. It is worth noting that there was no increase in the mean volume weighted crystallite size of the monazite structure in the Y25% sample after 28 days of HT ( $D \approx 20$  nm).

Figure 7 shows TEM image of nanoparticles and their distribution in the cross-sectional sizes of a sample with a composition of  $\text{La}_{0.75}\text{Y}_{0.25}\text{PO}_4$  with monazite structure after 28 days of HT. The monazite nanoparticles have rod-like shapes with a relatively high aspect ratio. The distribution of particles according to their smaller dimensions ranges from 10 to 40 nm, with a weighted average thickness of about 18 nm. It should be noted that a significant systematic error was most likely introduced into the particle size distribution during the sample preparation. It is due to the fact that upon completion of the ultrasonic dispersion of a suspension of particles in alcohol, the particles begin to settle to the bottom and the settling rate of large heavy particles is obviously higher. Nevertheless, the mean volume weighted crystallite size determined from the X-ray diffraction line profile ( $D = 20 \pm 8$  nm) correlates well with the TEM data on the average particle thickness.

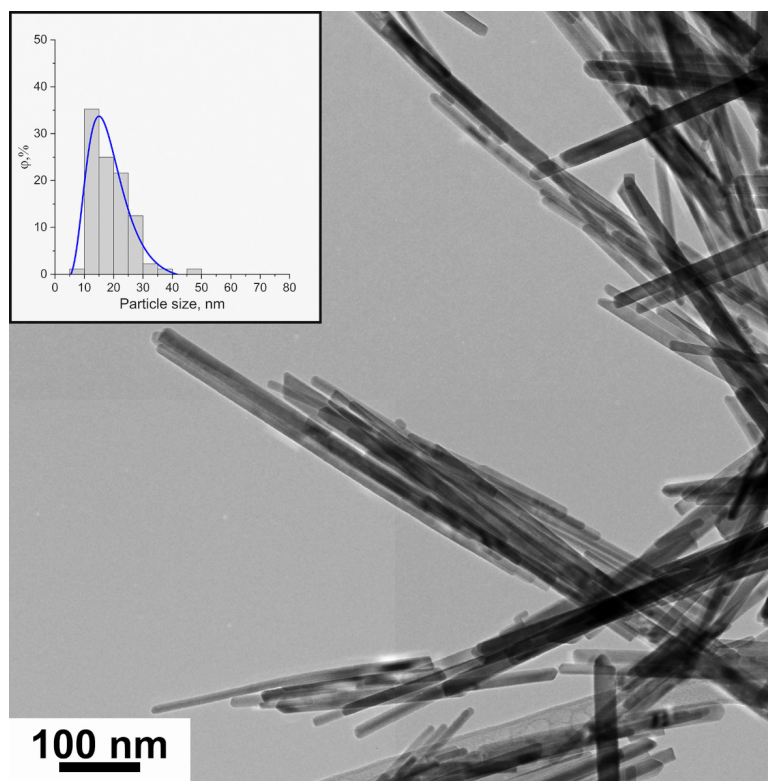


FIG. 7. TEM image of the  $\text{La}_{0.75}\text{Y}_{0.25}\text{PO}_4$  sample synthesized by the hydrothermal method at  $230^\circ\text{C}$  for 28 days and the histogram of particle size distribution (on inset)

Hydrothermal treatment at  $230^\circ\text{C}$  for 28 days leads to the formation of phases with compositions close to the equilibrium state of the system: a monazite-structured phase  $\text{La}_{1-x}\text{Y}_x\text{PO}_4$  ( $x \leq 0.03$ ) and a xenotime-structured phase  $\text{YPO}_4$ .

With increasing isothermal holding time of HT from 2 hours to 7 days and 28 days, a transformation of the rhabdophane-structured phase into the monazite-structured and xenotime-structured phases was observed in the system, along with a gradual redistribution of the  $\text{YPO}_4$  component between the monazite-structured and xenotime-structured phases. The  $\text{La}_{0.75}\text{Y}_{0.25}\text{PO}_4$  sample, crystallizing in the monazite-structured phase, does not change its phase composition or crystal size ( $D \approx 20$  nm) with increasing duration of isothermal holding time under hydrothermal condition. Based on the obtained data, it can be presumed that the  $\text{La}_{0.75}\text{Y}_{0.25}\text{PO}_4$  sample also crystallizes in a metastable monazite-structured phase, and that increasing the duration of HT will lead to transformations of this metastable phase into phases with more equilibrium compositions, such as the monazite-structured and xenotime-structured phases. On the other hand, analysis of literature data for the  $\text{LaPO}_4\text{--YPO}_4$  system at  $T \geq 1000^\circ\text{C}$  [46, 48] has shown that only one phase with a monazite structure is observed for the  $\text{La}_{0.75}\text{Y}_{0.25}\text{PO}_4$  sample. It is likely that the stability of the monazite-structured phase  $\text{La}_{0.75}\text{Y}_{0.25}\text{PO}_4$  is related to the prehistory of the initial sample and homogenization of the La and Y atoms in the rhabdophane-structured phase. However, without a phase diagram for the  $\text{LaPO}_4\text{--YPO}_4\text{--}(\text{H}_2\text{O})$  system, extrapolating the literature data to low temperature ranges would still have significant uncertainty.

#### 4. Conclusions

It has been shown that in the  $\text{LaPO}_4\text{--YPO}_4\text{--}(\text{H}_2\text{O})$  system, nanocrystalline samples of a solid solution with rhabdophane structure  $\text{La}_{1-x}\text{Y}_x\text{PO}_4 \cdot n\text{H}_2\text{O}$  ( $0 \leq x \leq 0.80$ ) were obtained using a precipitation method. The average thickness of the nanocrystals with rhabdophane structure correlates well with the mean volume weighted crystallite size for the samples after precipitation, indicating their single-crystalline structure in cross-sectional size of the nanorods. After hydrothermal treatment at  $230^\circ\text{C}$  for 2 hours, phases with monazite, rhabdophane, and xenotime structures are formed in the system in various ratios. After hydrothermal synthesis for 7 days in the system, phase transformation from a rhabdophane-structured phase to nanocrystals of two different compositions with monazite structure and to a xenotime-structured phase occurs. The phase fraction of the metastable phase with higher yttrium solubility in monazite structure after 7 days of HT ranged from  $\sim 20$  to  $\sim 35\%$ . With an increase in the duration of isothermal holding time to 28 days, the metastable phase with higher yttrium solubility in monazite structure is completely transformed into phases with structures of  $\text{YPO}_4$  xenotime and  $\text{La}_{1-x}\text{Y}_x\text{PO}_4$  monazite with compositions close to equilibrium.

Thus, it is shown that in the  $\text{LaPO}_4\text{--YPO}_4\text{--H}_2\text{O}$  system at low temperatures, the phase with variable composition with a high yttrium content and a monazite structure, and the phase of indefinite composition containing a significant amount of lanthanum with a rhabdophane structure, are not in equilibrium. The stability of the monazite phase in a sample with a composition of  $\text{La}_{0.75}\text{Y}_{0.25}\text{PO}_4$  after 2 hours, 7 days and 28 days of HT at  $230^\circ\text{C}$ , which does not change its composition and remains in the form of nanocrystals with an average crystal size of about 20 nm, can be explained by the presence of this phase in a metastable state.

#### References

- [1] Pawłó J., Zdończyk M., Guzik M., Boulon G., Guyot Y., Wilk-Kozubek M., Mudring A.-V., Cybińska J. Influence of ionic liquid and oleic acid assisted methods on the spectroscopic properties of  $\text{Nd}^{3+}$ -doped  $\text{GdPO}_4$  nano-particles. *J. Mater. Chem.*, 2023, **11**(22), P. 7227–7242.
- [2] Bouddouch A., Amaterz E., Taoufyq A., Bakiz B., Guinneton F., Villain S., Valmalette J.C., Gavarrí J.R., Benlhachemi A. Photocatalytic and photoluminescent properties of a system based on  $\text{SmPO}_4$  nanostructure phase. *Mater. Today Proc.*, 2020, **27**(4), P. 3139–3144.
- [3] Kahouadji B., Guerbous L., Boukerika A., Dolić S.D., Jovanović D.J., Dramićanin M.D. Sol gel synthesis and pH effect on the luminescent and structural properties of  $\text{YPO}_4\text{:Pr}^{3+}$  nanophosphors. *Opt. Mater.*, 2017, **70**, P. 138–143.
- [4] Yang J., Wang X., Song L., Luo N., Dong J., Gan S., Zou L. Tunable luminescence and energy transfer properties of  $\text{GdPO}_4\text{:Tb}^{3+}$ ,  $\text{Eu}^{3+}$  nanocrystals for warm-white LEDs. *Opt. Mater.*, 2018, **85**, P. 71–78.
- [5] Zhao R., Chen Z., Li Q., Wang X., Tang Y., Fu G., Li H., Lee J.M., Huang S. N-doped  $\text{LaPO}_4$ : An effective Pt-free catalyst for electrocatalytic oxygen reduction. *Chem Catal.*, 2022, **2**(12), P. 3590–3606.
- [6] Ramesh K., Zheng J., Ling E.G.Y., Han Y.F., Borgna A. Synthesis, Characterization and Catalytic Activity of Uniformly Crystalline  $\text{LaPO}_4$  Nanofiber Catalysts for Ethanol Dehydration. *J. Phys. Chem. C*, 2009, **113**(37), P. 16530–16537.
- [7] Woodward J., Kennel S.J., Stuckey A., Osborne D., Wall J., Rondinone A.J., Standaert R.F., Mirzadeh S.  $\text{LaPO}_4$  nanoparticles doped with actinium-225 that partially sequester daughter radionuclides. *Bioconjug. Chem.*, 2011, **22**(4), P. 766–776.
- [8] Sadowska K., Ragiń T., Kochanowicz M., Miluski P., Dorosz J., Leśniak M., Dorosz D., Kuwik M., Pisarska J., Pisarski W., Rećko K., Żmojda J. Analysis of Excitation Energy Transfer in  $\text{LaPO}_4$  Nanophosphors Co-Doped with  $\text{Eu}^{3+}/\text{Nd}^{3+}$  and  $\text{Eu}^{3+}/\text{Nd}^{3+}/\text{Yb}^{3+}$ . *Ions. Mater.*, 2023, **16**(4), P. 1588.
- [9] Zhang L., Bai S., You H., Wu H., Peng Q., Li W., Cao K., Zhou Y. Submicrometre-sized  $\text{EuPO}_4$  hollow spheres: template-directed synthesis and luminescent properties. *Micro Nano Lett.*, 2019, **14**(3), P. 309–312.
- [10] Michel C.R., Martínez-Preciado A.H., Rivera-Tello C.D.  $\text{CO}_2$  gas sensing response of  $\text{YPO}_4$  nanobelts produced by a colloidal method. *Sensors Actuators B Chem.*, 2015, **221**, P. 499–506.
- [11] Zhang P., Wang E., Guo C., Yang T., Hou X. High-entropy rare earth phosphates ( $\text{REPO}_4$ , RE = Ho, Tm, Yb, Lu, Dy, Er and Y) with excellent comprehensive properties. *J. Eur. Ceram. Soc.*, 2023, **35**(12), P. 2892–2896.
- [12] Mezentseva L.P., Osipov A.V., Ugolkov V.L., Koptelova L.A., Khamova T.V. Comparative Study of the Synthesis of Ceramic Composites Based on Lanthanum Orthophosphate. *Glas. Phys. Chem.*, 2023, **49**, P. 379–385.
- [13] Yorov K.E., Shekunova T.O., Baranchikov A.E., Koptitsa G.P., Almásy L., Skogareva L.S., Kozik V.V., Malkova A.N., Lermontov S.A., Ivanov V.K. First rare-earth phosphate aerogel: sol–gel synthesis of monolithic ceric hydrogen phosphate aerogel. *J. Sol-Gel Sci. Technol.*, 2018, **85**, P. 574–584.
- [14] Chaudan E., Kim J., Tusseau-Nenez S., Goldner P., Malta O.L., Peretti J., Gacoin T. Polarized Luminescence of Anisotropic  $\text{LaPO}_4\text{:Eu}$  Nanocrystal Polymorphs. *J. Am. Chem. Soc.*, 2018, **140**(30), P. 9512–9517.

- [15] Makowski M., Witkowski M.E., Drozdowski W., Wojtowicz A.J., Wisniewski K., Boatner L.A. Luminescence and scintillation properties of  $\text{XPO}_4\text{:Nd}^{3+}$  (X = Y, Lu, Sc, La) crystals. *Opt. Mater.*, 2018, **79**, P. 273–278.
- [16] Mezentseva L.P., Osipov A.V., Ugolkov V.L., Akatov A.A., Doil'nitsyn V.A. Physicochemical Properties of Ceramics Based on a  $\text{LaPO}_4\text{--DyPO}_4$  System. *Glas. Phys. Chem.*, 2019, **45**, P. 268–271.
- [17] Heuser J.M., Palomares R.I., Bauer J.D., Rodriguez M.J.L., Cooper J., Lang M., Scheinost A.C., Schlenz H., Winkler B., Bosbach D., Neumeier S., Deissmann G. Structural characterization of (Sm,Tb) $\text{PO}_4$  solid solutions and pressure-induced phase transitions. *J. Eur. Ceram. Soc.*, 2018, **38**(11), P. 4070–4081.
- [18] Kamel N., Remil K., Arabi M., Kamel Z., Zahri A., Metahri S. Effect of the synthesis method on the properties of a Pb-bearing (Y–Gd–Ce) rare-earth phosphate used for the confinement of high-level radioactive waste. *J. Nucl. Mater.*, 2010, **401**(1-3), P. 104–112.
- [19] Ni Y., Hughes J.M., Mariano A.N. Crystal chemistry of the monazite and xenotime structures. *Am. Mineral.*, 1995, **80**(1-2), P. 21–26.
- [20] Heuser J.M., Neumeier S., Peters L., Schlenz H., Bosbach D., Deissmann G. Structural characterisation of metastable Tb- and Dy-monazites. *J. Solid State Chem.*, 2019, **273**, P. 45–52.
- [21] Kijkowska R. Thermal decomposition of lanthanide orthophosphates synthesized through crystallisation from phosphoric acid solution. *Thermochim. Acta.*, 2003, **404**(1-2), P. 81–88.
- [22] Mooney R.C.L. X-ray diffraction study of cerous phosphate and related crystals. I. Hexagonal modification. *Acta Crystallogr.*, 1950, **3**, P. 337–340.
- [23] Mesbah A., Clavier N., Elkaim E., Szenknect S., Dacheux N. In pursuit of the rhabdophane crystal structure: from the hydrated monoclinic  $\text{LnPO}_4 \cdot 0.667\text{H}_2\text{O}$  to the hexagonal  $\text{LnPO}_4$  (Ln = Nd, Sm, Gd, Eu and Dy). *J. Solid State Chem.*, 2017, **249**, P. 221–227.
- [24] Subramani T., Rafiuddin M.R., Shelyug A., Ushakov S., Mesbah A., Clavier N., Qin D., Szenknect S., Elkaim E., Dacheux N., Navrotsky A. Synthesis, Crystal Structure and Enthalpies of Formation of Churchite-type  $\text{REPO}_4 \cdot 2\text{H}_2\text{O}$  (RE = Gd to Lu) Materials. *Cryst. Growth Des.*, 2019, **19**(8), P. 4641–4649.
- [25] Hikichi Y., Sasaki T., Murayama K., Nomura T., Miyamoto M. Mechanochemical Changes of Weinschenkite-Type  $\text{RPO}_4 \cdot 2\text{H}_2\text{O}$  (R = Dy, Y, Er, or Yb) by Grinding and Thermal Reactions of the Ground Specimens. *J. Am. Ceram. Soc.*, 1989, **72**(6), P. 1073–1076.
- [26] Ivashkevich L.S., Lyakhov A.S., Selevich A.F. Preparation and structure of the yttrium phosphate dihydrate  $\text{YPO}_4 \cdot 2\text{H}_2\text{O}$ . *Phosphorus Res. Bull.*, 2013, **28**, P. 45–50.
- [27] Shelyug A., Mesbah A., Szenknect S., Clavier N., Dacheux N., Navrotsky A. Thermodynamics and stability of rhabdophanes, hydrated rare earth phosphates  $\text{REPO}_4 \cdot n\text{H}_2\text{O}$ . *Front. Chem.*, 2018, **6**, P. 604.
- [28] Ochiai A., Utsunomiya S. Crystal Chemistry and Stability of Hydrated Rare-Earth Phosphates Formed at Room Temperature. *Miner.*, 2017, **7**(5), P. 84.
- [29] Hikichi Y., Ota T., Hattori T., Imaeda T. Synthesis and Thermal Reactions of Rhabdophane-(Y). *Mineral. J.*, 1996, **18**(3), P. 87–96.
- [30] Bryukhanova K.I., Nikiforova G.E., Gavrichev K.S. Synthesis and study of anhydrous lanthanide orthophosphate (Ln = La, Pr, Nd, Sm) nanowhiskers. *Nanosystems: Phys. Chem. Math.*, 2016, **7**(3), P. 451–458.
- [31] Enikeeva M.O., Proskurina O.V., Motaylo E.S., Danilovich D.P., Gusarov V.V. The influence of condition of the monazite structured  $\text{La}_{0.9}\text{Y}_{0.1}\text{PO}_4$  nanocrystals sintering on thermal and mechanical properties of the material. *Nanosystems: Phys. Chem. Math.*, 2021, **12**(6), P. 799–807.
- [32] Proskurina O.V., Sivtsov E.V., Enikeeva M.O., Sirotkin A.A., Abiev R. Sh., Gusarov V.V. Formation of rhabdophane-structured lanthanum orthophosphate nanoparticles in an impinging-jets microreactor and rheological properties of sols based on them. *Nanosystems: Phys. Chem. Math.*, 2019, **10**(2), P. 206–214.
- [33] Rafiuddin M.R., Tyagi C., Haq M.A. Synthesis and structural investigation of churchite-type  $\text{REPO}_4 \cdot 2\text{H}_2\text{O}$  (RE = Y, Gd, Dy) nanocrystals. *J. Solid State Chem.*, 2022, **311**, P. 123150.
- [34] Lucas S., Champion E., Bregiroux D., Bernache-Assollant D., Audubert F. Rare earth phosphate powders  $\text{RePO}_4 \cdot n\text{H}_2\text{O}$  (Re=La, Ce or Y)—Part I. Synthesis and characterization. *J. Solid State Chem.*, 2004, **177**(4-5), P. 1302–1311.
- [35] Sankar S., Warriar K.G. Aqueous sol-gel synthesis of lanthanum phosphate nano rods starting from lanthanum chloride precursor. *J. Sol-Gel Sci. Technol.*, 2011, **58**, P. 195–200.
- [36] Mezentseva L.P., Osipov A.V., Ugolkov V.L., Akatov A.A., Doil'nitsyn V.A., Maslennikova T.P., Yakovlev A.V. Sol-Gel Synthesis, Thermal Behavior of Nanopowders and Chemical Stability of  $\text{La}_{1-x}\text{Ho}_x\text{PO}_4$  Ceramic Matrices. *Glas. Phys. Chem.*, 2018, **44**, P. 440–449.
- [37] Ugolkov V.L., Mezentseva L.P., Osipov A.V., Popova V.F., Maslennikova T.P., Akatov A.A., Doil'nitsyn V.A. Synthesis of nanopowders and physicochemical properties of ceramic matrices of the  $\text{LaPO}_4\text{--YPO}_4\text{--(H}_2\text{O)}$  and  $\text{LaPO}_4\text{--HoPO}_4\text{--(H}_2\text{O)}$  systems. *Russ. J. Appl. Chem.*, 2017, **90**, P. 28–33.
- [38] Ahmadzadeh M.A., Chini S.F., Sadeghi A. Size and shape tailored sol-gel synthesis and characterization of lanthanum phosphate ( $\text{LaPO}_4$ ) nanoparticles. *Mater. Des.*, 2019, **181**, P. 108058.
- [39] Colomer M.T., Ortiz A.L., Effect of  $\text{Tb}^{3+}$  doping and self-generated pressure on the crystallographic/morphological features and thermal stability of  $\text{LaPO}_4 \cdot n\text{H}_2\text{O}$  single-crystal nanorods obtained by microwave-assisted hydrothermal synthesis. *Ceram. Int.*, 2016, **42**(16), P. 18074–18086.
- [40] Palma-Ramírez D., Domínguez-Crespo M.A., Torres-Huerta A.M., Dorantes-Rosales H., Ramírez-Meneses E., Rodríguez E. Microwave-assisted hydrothermal synthesis of  $\text{CePO}_4$  nanostructures: Correlation between the structural and optical properties. *J. Alloys Compd.*, 2015, **643**, P. S209–S218.
- [41] Enikeeva M.O., Kenges K.M., Proskurina O.V., Danilovich D.P., Gusarov V.V. Influence of Hydrothermal Treatment Conditions on the Formation of Lanthanum Orthophosphate Nanoparticles of Monazite Structure. *Russ. J. Appl. Chem.*, 2020, **93**, P. 540–548.
- [42] Meyssamy H., Riwtzki K., Kornowski A., Naused S., Haase M. Wet-Chemical Synthesis of Doped Colloidal Nanomaterials: Particles and Fibers of  $\text{LaPO}_4\text{:Eu}$ ,  $\text{LaPO}_4\text{:Ce}$  and  $\text{LaPO}_4\text{:Ce,Tb}$ . *Adv. Mater.*, 1999, **11**(10), P. 840–844.
- [43] Leys J.M., Ji Y., Klinkenberg M., Kowalski P.M., Schlenz H., Neumeier S., Bosbach D., Deissmann G. Monazite-Type  $\text{SmPO}_4$  as Potential Nuclear Waste Form: Insights into Radiation Effects from Ion-Beam Irradiation and Atomistic Simulations. *Materials*, 2022, **15**(10), P. 3434
- [44] Lucas S., Champion E., Bernache-Assollant D., Leroy G. Rare earth phosphate powders  $\text{RePO}_4 \cdot n\text{H}_2\text{O}$  (Re=La, Ce or Y) II. Thermal behavior. *J. Solid State Chem.*, 2004, **177**(4-5), P. 1312–1320.
- [45] Enikeeva M.O., Proskurina O.V., Levin A.A., Smirnov A.V., Nevedomskiy V.N., Gusarov V.V. Structure of  $\text{Y}_{0.75}\text{La}_{0.25}\text{PO}_4 \cdot 0.67\text{H}_2\text{O}$  rhabdophane nanoparticles synthesized by the hydrothermal microwave method. *J. Solid State Chem.*, 2023, **319**, P. 123829.
- [46] Mogilevsky P., Boakye E.E., Hay R.S. Solid solubility and thermal expansion in a  $\text{LaPO}_4\text{--YPO}_4$  system. *J. Am. Ceram. Soc.*, 2007, **90**(6), P. 1899–1907.
- [47] Emden B. V., Thornber M., Graham J., Lincoln F.J. Solid Solution Behaviour of Synthetic Monazite and Xenotime from Structure. Proceeding of “45th Annual Denver X-ray Conference”. Denver, Colorado, USA, 1996.
- [48] Mogilevsky P. On the miscibility gap in monazite-xenotime systems. *Phys. Chem. Miner.*, 2007, **34**, P. 201–214.
- [49] Enikeeva M.O., Proskurina O.V., Danilovich D.P., Gusarov V.V. Formation of nanocrystals based on equimolar mixture of lanthanum and yttrium orthophosphates under microwave-assisted hydrothermal synthesis. *Nanosystems: Phys. Chem. Math.*, 2020, **11**(6), P. 705–715.

- [50] Scherrer P. Bestimmung der Größe und der inneren Struktur von Kolloidteilchen mittels Röntgenstrahlen. *Nachrichten von Der Gesellschaft Der Wissenschaften Zu Göttingen Math.Klasse.*, 1918, P. 98–100.
- [51] Retgers J. W. The Specific Gravity of Isomorphic Mixtures. *Zeitschrift Für Phys. Chemie.*, 1889, **3**, P. 497–497.

---

*Submitted 10 October 2023; revised 15 November 2023; accepted 16 November 2023*

*Information about the authors:*

*Maria O. Enikeeva* – Ioffe Institute, 194021 St. Petersburg, Russia; St. Petersburg State Institute of Technology, 190013 St. Petersburg, Russia; ORCID 0000-0002-9633-4421; odin2tri45678@gmail.com

*Olga V. Proskurina* – Ioffe Institute, 194021 St. Petersburg, Russia; St. Petersburg State Institute of Technology, 190013 St. Petersburg, Russia; ORCID 0000-0002-2807-375X; proskurinaov@mail.ru

*Evgeny Yu. Gerasimov* – Federal Research Center, Boreskov Institute of Catalysis SB RAS, Novosibirsk 630090, Russia; ORCID 0000-0002-3230-3335; gerasimov@catalysis.ru

*Vladimir N. Nevedomskiy* – Ioffe Institute, 194021 St. Petersburg, Russia; ORCID 0000-0002-7661-9155; nevedom@mail.ioffe.ru

*Victor V. Gusarov* – Ioffe Institute, 194021 St. Petersburg, Russia; ORCID 0000-0003-4375-6388; gusarov@mail.ioffe.ru

*Conflict of interest:* the authors declare no conflict of interest.